HHS Public Access

Author manuscript

J Neural Eng. Author manuscript; available in PMC 2023 November 14.

Published in final edited form as:

J Neural Eng. ; 19(2): . doi:10.1088/1741-2552/ac697c.

Angle-tuned coils: attractive building blocks for TMS with improved depth-spread performance

Hedyeh Bagherzadeh[1,5], **Qinglei Meng**[2,5], **Zhi-De Deng**[3], **Hanbing Lu**[2], **Elliott Hong**[4], **Yihong Yang**[2], **Fow-Sen Choa**[1,*]

[1]Department of Computer Science and Electrical Engineering, University of Maryland, Baltimore, MD, United States of America

[2]Magnetic Resonance Imaging and Spectroscopy, National Institute on Drug Abuse, Intramural Research Programs, National Institutes of Health, Baltimore, MD, United States of America

[3]Noninvasive Neuromodulation Unit, Experimental Therapeutics and Pathophysiology Branch, National Institute of Mental Health, National Institutes of Health, Bethesda, MD, United States of America

[4]Maryland Psychiatric Research Center, Department of Psychiatry, University of Maryland School of Medicine, Baltimore, MD, United States of America

[5]Co-first Author

Abstract

Objective.—A novel angle-tuned ring coil is proposed for improving the depth-spread performance of transcranial magnetic stimulation (TMS) coils and serve as the building blocks for high-performance composite coils and multisite TMS systems.

Approach.—Improving depth-spread performance by reducing field divergence through creating a more elliptical emitted field distribution from the coil. To accomplish that, instead of enriching the Fourier components along the planarized (*x*-*y*) directions, which requires different arrays to occupy large brain surface areas, we worked along the radial (*z*) direction by using tilted coil angles and stacking coil numbers to reduce the divergence of the emitted near field without occupying large head surface areas. The emitted electric field distributions were theoretically simulated in spherical and real human head models to analyze the depth-spread performance of proposed coils and compare with existing figure-8 coils. The results were then experimentally validated with field probes and *in-vivo* animal tests.

Main results.—The proposed 'angle-tuning' concept improves the depth-spread performance of individual coils with a significantly smaller footprint than existing and proposed coils. For composite structures, using the proposed coils as basic building blocks simplifies the design and manufacturing process and helps accomplish a leading depth-spread performance. In addition,

*Author to whom any correspondence should be addressed. choa@umbc.edu.

Conflict of interest

Elliott Hong, Fow-Sen Choa, and Qinglei Meng have patents or/and patent applications that include aspects of the research presented in this paper. The other authors declare no conflict of interest.

Supplementary material for this article is available online

the footprint of the proposed system is intrinsically small, making them suitable for multisite stimulations of inter and intra-hemispheric brain regions with an improved spread and less electric field divergence.

Significance.—Few brain functions are operated by isolated single brain regions but rather by coordinated networks involving multiple brain regions. Simultaneous or sequential multisite stimulations may provide tools for mechanistic studies of brain functions and the treatment of neuropsychiatric disorders. The proposed AT coil goes beyond the traditional depth-spread tradeoff rule of TMS coils, which provides the possibility of building new composite structures and new multisite TMS tools.

Keywords

TMS; electric field; stimulation depth; spread; decay rate; AT coil

1. Introduction

Administration (FDA) treatment for major depression disorder, migraine, and obsessive-compulsive disorder [1, 2]. The applications of TMS have been further extended to areas that cover brain connectivity, cognitive, perceptual, behavioral, and therapeutic transcranial magnetic stimulation (TMS) is a rapidly evolving non-invasive neuromodulation technique and an established U.S. Food and Drug investigations, and treatment [3–5]. Since normal and pathological brain functions involve multiple brain networks, and each brain network contains multiple sub-regions [6, 7], tools like dual-coil TMS can provide exceptional opportunities to investigate effective connectivity and plasticity through the ability to utilize excitatory or inhibitory stimulations to change long-term potentiation and long-term depression of interconnected brain regions [8–12]. Multisite neuromodulation with controlled timing provides a tool for mechanistic studies of coordinated brain dynamics, complex gating effect in humans, and validating brain connectivity biomarkers, in addition to the treatment of neurologic and psychiatric disorders [13–16]. However, conventional circular and figure-8 TMS coils occupy a substantial footprint, defined here as the tangential surface area the coil occupies in the contact surface plane closest to the head. Therefore, it is challenging to accomplish more than two stimulation sites with the flexibility to move the coils around and reach the desired locations. Due to the large size of the stimulating coils, the multisite stimulation is predominantly focused on inter-hemispheric connectivity between brain regions [17, 18]. This complication cannot be resolved by shrinking the coil size to accommodate the space congestion challenge since the smaller conventional coils have higher field divergence characteristics, preventing them from providing sufficient field intensity for a suprathreshold stimulation at a typical depth for the human cortex.

There have been consistent efforts to reduce field divergence and increase field strength to reach deep brain regions with a small spread. Since field emission from TMS coils is low frequency and near-field, the coils' geometric arrangement is crucial in shaping the emitted field distribution. Various TMS coil geometries have been adopted along with additional methods for field divergence improvement [19–25]. To optimize the TMS coil's electric field distribution, theoretical analysis based on analytical models [26–29] or numerical simulations using either finite element method (FEM) or finite difference method [30–37]

have been implemented along with additional physical and experimental verifications [38–40] and rodent experiments [41–43]. The coil performance is generally governed by a depth¬–spread tradeoff [25]. Larger aperture coils have a smaller field divergence and can reach deeper regions with a slower field decay rate; however, the field spread is already significant when initiated from the aperture. On the other hand, smaller aperture coils have a more substantial field divergence; it quickly spreads with a faster field decay rate even though the field spread is initially small.

Geometric shaping of the electric field can also be accomplished using multiple coils to achieve a less spread field distribution. As a result, the field distribution in the head has a more elliptical shape than just spherical, and deeper stimulation depth can be accomplished with a smaller tangential field spread. Based on such a concept, using coils with different sizes and polarities to trim the combined near field elements has been proposed [22, 44, 45]. Notably, in Meng *et al*'s work, field-shaping using an array of passive rings has the advantage of simplicity, requiring only one power supply and less energy consumption [45]. However, the trimming is less controllable compared with shaping through active elements. Gomez *et al* [22] used arrays of coils with large and small diameters to enrich spatial Fourier components and accomplish a sharper near-field spatial distribution with enhanced depth and reduced spread. The spherical harmonics are built up along the curved plane of a head model. There is a limited improvement in the efficacy of the planarized spatial components to optimize (sharpen) the distribution along the radial (perpendicular) direction with no spatial components in this direction in the emitted near-field. Furthermore, using active elements for field-shaping needs accurate control of the counter field in large and small coils to adjust the Fourier coefficient of each spatial harmonic component; with such counter field design, more power consumption is needed. In addition, these approaches require the coil to have a high occupied surface area on the scalp for a single site stimulation [22] and present a challenge for multisite stimulation applications.

The importance of multisite stimulation of different brain regions has culminated in various coil designs for this purpose. De Lara *et al* [46] proposed a three-axis coil design for multichannel stimulation providing accurate electric field steerability and targeting, which can be used in concurrent TMS–fMRI studies. Simultaneous control of multiple power supplies, each with a different setting, may make the emitted field different from the simulations. The stimulation depth may also be restricted by the smaller size coils. Koponen *et al* [47] designed a five-coil multi-locus apparatus to accomplish controlling the stimulation location. The designed coil comprises stacked layers of orthogonally-oriented figure-8, cloverleaf, and circular coils with a substantial tangential footprint. The steerable portion of the induced field lies at the stack's center and could not cover a larger cortex area.

In this work, novel angle-tuned (AT) ring coils are proposed to reduce the individual coil footprint and improve depth–spread characteristics. The field-shaping technique and the structure are simple and do not require counter-field generations, making it easy to implement and modify. Stacking multiple coils enhances field strength, reduces the footprint, and increases the field penetration depth by modifying its geometric distribution. By manipulating the coils' composite structure along the Z-direction, we have induced a sharper elliptical electric field distribution and enhanced electric field strength through the

superposition of the stacked coils. Increasing the coil wire-wrapping angle reduces the field spread by introducing asymmetry to the proposed coils' simple structure. Below we present theoretical and experimental comparisons of a commercial figure-8 coil's field emission distributions with multi-stacked and AT coils. In addition, the AT coils were used to perform *in-vivo* stimulation of a rat and a mouse brain to show their improved performance and capability for brain stimulation. These novel coils demonstrated better spread, higher electric field penetration, better field decay rate, and smaller footprints than conventional coils, making them suitable for studies on enter and intra-hemispheric interactions in the brain's neural network.

2. Methods and experiments

2.1. COMSOL FEM simulations

We used the AC/DC module of COMSOL (COMSOL Multiphysics, Version 5.5) to calculate the induced electric field characteristics generated by the AT coils. To help quantitatively compare the depth-spread performance with other existing coils, a uniform spherical head model with a 17 cm diameter and isotropic electrical conductivity of 0.33 S m^{-1} was used [25]. One shall notice that for evaluating TMS coils' emission patterns, it is not appropriate to use realistic head models, which are aimed at studying TMS's medical effects on the brain. For the purpose of comparing the performance of different TMS coil designs, using a nonspecific spherical head model is more appropriate since it does not produce a bias toward a particular brain size or shape. The evaluation results will be valid for and can later be applied to all different brain geometries. It has also been shown that besides adding the burden of more calculation time, there is little difference in using the realistic head model or using spherical models in terms of coil performance evaluation [48, 49]. So, in this study, we employed the spherical model to quantitively compare the depth-spread performance of AT coils with existing coils. We will then calculate field distribution based on a realistic head model to graphically illustrate the difference between using AT coils and commercial figure-8 coils in multisite TMS tool implementation.

Figure 1(a) illustrates our TMS coil design. The coil has a fixed winding width (the difference between the outer and inner diameters) of 1 cm. In the simulations, we used a variety of the windings' inner and outer diameters. We changed the coil stacking number from 2 to 5 and then to 9 along the central axis (Z-axis) with a tilting angle of up to 70° with a total height of 12.0 cm, 21.8 cm, and 34.8 cm, respectively. The layers are connected in series; the current excitation in all coils is a sinusoidal wave with a frequency of 5 kHz. A 0.5 cm layer of insulation has been considered for the coil and is placed between the coil and the head surface. The COMSOL settings and equations are further explained in the supplementary data (available online at stacks.iop.org/JNE/19/026059/mmedia).

2.2. Stimulation depth and spread

Figures 1(b) and (c) illustrate the definition of stimulation depth and spread in the head model introduced by the half-value depth ($d_{1/2}$), half-value spread ($S_{1/2}$), and half-value volume ($V_{1/2}$) described in Deng *et al* [25]. To calibrate our COMSOL simulations with previous studies, we selected three coils and used the same coil parameters in Deng *et al*

[25]. The half-value depth and spread of the three coils were analyzed: 70 mm circular (#4), 70 mm figure-8 (#31), and double cone (#37) Magstim coil. For all three cases, our simulated depth–spread results are within 1% of previously reported [25] results, as shown in figure S1 in the supplementary data. We have also included other simulation results from Deng *et al* [25] in the depth-spread plot to form the best-fit curves for circular coils (solid line) and figure-8 coils (dashed line). We use the two curves as references to illustrate how different coil design parameters, such as tilting angle, number of winding layers, coil location, rotation angle, and outer diameter size, can affect the performance in terms of locations in the $S_{1/2}$ vs. $d_{1/2}$ plot. The plot's maximum points for $S_{1/2}$ and $d_{1/2}$ have been defined by exposing the spherical head model to the induced field from a symmetric spherical coil covering the whole head [25]. We further compare both simulation and experimental results of a commercial figure-8 coil and two of our AT coils with different coil diameters and tilting angles and show their field intensities and spot sizes at different distances from the coil.

2.3. Footprint of AT coils

Figure 1(d) demonstrates the footprint definition, characterized as the tangential surface area that the coil occupies in the projected surface plane. For example, the 70 mm figure-8 Magstim coil has a lateral surface area of 120 cm^2, making it challenging to operate more than two of these coils on the human head simultaneously due to size limitations. For the proposed AT coils, the footprint is the coil's projection area on the head model surface, dependent on the tilting angle. For example, the AT coil with an outer diameter of 4.5 cm has a footprint range of 5.5 cm^2 to 15.9 cm^2 when the tilted angle changes from 70° to 0°—a flat coil. Thus, the footprint for the 70° tilted coil is approximately 95% less than the figure-8 coil. The smaller footprint of the coils allows more coils to be operated over the head for multisite stimulation.

2.4. Prototype fabrication and electric field measurements

In our experimental works, AT coils were fabricated using wire-wrapping over 3D printed coil holders, which were printed with different angles and dimensions. The wires are made of Litz wire bundles with 135 pieces of insulated AWG30 wires for flexible bending and high current operations. Figure 1(e) shows the manufactured coil for the experimental measurements. The fabricated coil's weight, even insulated in epoxy, is suitable for any coil support stand. A Magstim 200 (Magstim Co Ltd, Whitland, UK.) stimulator was used to drive these coils with the power set at 30% during the measurements, producing about 480 V on the discharging capacitor. Using a 30% power rating to conduct the field distribution measurements is necessary since it obtains reliable results while not pushing the instrument to its operation lifetime limit due to the high number of trials. The coil's electric field distribution was measured in the air with a 5 mm step using calibrated high-spatial-resolution vector-field probes [50]. Since adding the variation of cerebrospinal fluid (CSF) conductivity uniformly in the head model does not significantly influence the field convergence or divergence, we did not consider measuring the field distribution in a CSF phantom. The total field strength, $|E| = \left(E_x^2 + E_y^2 + E_z^2\right)^{1/2}$, is obtained by measuring the x, y, and z -direction field components within the $X - Y$ planes at each step. We normalized

the obtained values for easy comparison between experimental and simulation results. Additional explanations regarding the experimental setup are provided in the supplementary data.

2.5. *In-vivo* animal experiment

To demonstrate the performance of the proposed coils, a set of *in-vivo* tests were performed on anesthetized mice (male C57BL/6 J mice $n = 6$) and rats. In these tests, the animals were anesthetized with sodium pentobarbital intraperitoneally. All the procedures are approved by the National Institute of Drug Abuse animal care and use committee. The coil used for this purpose had a tilting angle of 5°, an outer diameter of 25 mm, an inner diameter of 6 mm, and a total length of 150 mm and was fixated in epoxy. The coil was placed over the animal head using a micromanipulator and adjusted over the motor cortex to induce a twitch on the contralateral hindlimb. The stimulation results are demonstrated in two videos provided as supplementary videos.

3. Results and discussion

3.1. FEM simulations

Figure 2 illustrates the AT coils' performance with an inner diameter of 8 cm and an outer diameter of 9 cm with tilting angles ranging from 0 to 70° with 10° steps and stacking numbers of 2, 5, and 9. When the tilting angle is increased from 0° (circular coil stack) to 70°, the spread is significantly reduced with a slight reduction in the depth. The reduction in the depth may be due to the tilting effect since part of the coil is pulling away from the head model.

The coils' depth–spread performance surpasses the figure-8 coil curve when the tilting angle reaches about 50°–60° and beyond. This improvement clearly shows that the primary effect of the angle-tuning is to reduce the field spread. To check one numerical example, we compare the depth–spread of a five-winding-layer, 70° tilted coil with the 70 mm figure-8 Magstim coil (#31). They have a similar spread, but the AT coil has a 20% deeper half-depth and a smaller footprint by about 82%, as the figure-8 coil has a footprint of about 120 cm^2 and the AT coil has a footprint of 22 cm^2.

It is also demonstrated that when the coil stacking number increases, the depth performance improves. This effect seems to be saturated from five to nine windings. The overall thickness of the coil stacking along the z-axis, e.g. number of windings, has a non-linear relation with the penetration depth. As the AT coil winding number increases, the upper-windings do not contribute to the targeted stimulation electric field as efficiently as the lower windings due to the divergence of the magnetic flux. The ineffectiveness of additional windings in the coil's performance is determined by various parameters, including the coil's outer diameter, the thickness of each winding, and the tilting angle of the coil. Each of these parameters is individually discussed in the manuscript and the supplementary material.

Coil position and rotation to adjust the coil direction relative to the head model can also improve the depth–spread performance, as illustrated in figures S3 and S4 in the supplementary data. From this study, we can understand that the combination of coil

stacking and angle tuning has produced an elliptical electric field profile instead of a spherical distribution. If the coil is appropriately aligned with the head model, the induced electric field occupies a smaller volume.

To obtain the tradeoff curve, we vary the coils' outer diameter between 2 cm and 100 cm while keeping the winding width constant at 1 cm. The tilting angle was fixed at 70°, and the rotation angle was 20°, with the lower edge of the coil aligned with the head model's central axis. Figure 3 shows the results of these coils' depth–spread performance as a function of coil diameter. It should be noted that the larger coils are analyzed for comparison purposes and are not feasible for brain stimulation due to their dimension. The AT coils have a smaller footprint and demonstrate a better tradeoff curve than conventional figure-8 coils. For example, an AT coil with an inner and outer diameter of 3.5 cm and 4.5 cm, respectively, establishes the same $d_{1/2}$ as the figure-8 coil (coil #31) with a 10% smaller spread. When the coil's inner and outer diameters reach 8.0 cm and 9.0 cm, respectively, the half-value depth experienced a 20% increase compared to the figure-8 coil (coil #31) with the same spread ($S_{1/2}$). In addition, if compared with the double cone coil, the AT coil with an outer diameter of 20 cm demonstrates the same half-value depth but with a 20% smaller spread. This is a considerable improvement compared to the existing figure-8 coils, given that the AT coil occupies a significantly smaller footprint.

As shown, the most effective depth-enhancement method for the single AT coils is to increase the diameter of the wiring pattern. However, that negatively affects the focality of the electric field distribution. The performance of the single AT coils resembles that of circular coils with enhanced depth-spread values. The AT coils demonstrate enhancements in the circular coil by introducing asymmetry to the coil structure and adjusting the shape of the induced electric field distribution from spherical to elliptical.

AT coils can also be used as fundamental building blocks for coils with complex structures and better depth–spread performance. A single AT coil is not symmetric, and it can occupy more $V_{1/2}$ in the head model. Adding another AT coil to form a pair and having two AT coil pairs with opposite polarities can create a symmetric structure and produce a more elliptical field distribution. By adjusting various angles among these pairs, we can further optimize the depth–spread performance and obtain an even better depth–spread tradeoff curve. Figure 4 shows an implemented example using this concept. The AT coils' arrangement in the proposed structure is inserted in the top left corner with red arrows demonstrating each coil's current direction. In this design, two 80° tilted coils with an angle of 20° between them form a pair; the proposed coil design comprises two of these pairs with opposite polarities and an internal angle of 60° between them, and the coil I.D. changes from 3.5 to 29 cm with a 1 cm winding width. This result indicates a further improvement of the $S_{1/2}$ and $d_{1/2}$ and confirms AT coils' role as building blocks for complex coil structures. Compared with the commercial 70 mm figure-8 coil (coil #31), the 3.5 cm inner diameter four-AT-coil module demonstrates a 10% smaller spread and a 30% larger $d_{1/2}$. The design with a 5 cm inner diameter four-AT-coil module demonstrates a 15% larger spread and a 50% deeper $d_{1/2}$ than the corresponding figure-8 coil. The coil also has the same $d_{1/2}$ but a 40% smaller spread than the double cone coil. The proposed four-AT-coil composite structure demonstrates a better depth-spread performance than existing coils. The performance of the four-AT-coil

system resembles the slope of the figure-8 coils in the plots. The reason is the use of multiple coils to adjust the asymmetry in each AT coil and generate symmetric coils and an elliptical field distribution.

The AT coils have demonstrated a significant potential for multisite brain stimulation in comparison to conventional coils. Figure 5(a) illustrates the difficulty and impossibility of implementing more than two sites for multisite TMS tools using conventional figure-8 coils. The congestions caused by the overlapping of the coils are marked in red circles. The calculations for the analysis are done using a realistic head model to show the results of a four-coil multisite AT coil-based TMS tool and a commercial figure-8 dual coil system. The real human head model selected for this purpose is model No. 111 716 from the Population Head Model Repository [51, 52] available through IT'IS Foundation, Switzerland. The tissue electrical conductivity for each region (skin, skull, CSF, gray matter, white matter, cerebellum, and ventricles) was assigned based on [53]. The AT coils used in this analysis had an O.D. of 4.5 cm and an I.D. of 3.5 cm and were compared to the Magstim 70 mm figure-8 coil. As shown in figure 3, the two different coils have the same penetration depth while the AT coil demonstrates a reduced spread.

Figure 5(b) shows that using four AT coils has enabled simultaneous stimulation of four different regions of gray matter in the frontal lobe, occipital lobe, and temporal lobe with a limited spread for focal stimulation. In addition, the stimulation hot spot size and intensity on the head are minimal and restricted, which reduces the risk of seizure and burning sensation. The AT coils can further be used to stimulate multiple points in a single lobe due to their significantly small footprint. Figure 3(c) demonstrates the stimulation locations and results of dual figure-8 coils in the gray matter. As seen here, the hot spot size obtained with the AT coil is smaller than the figure-8 coil. As shown in figure S8 in the supplementary material, it should be noted that due to the induced electric field from adjacent coils, figure-8 coils can easily create unexpected stimulation unless the coil's direction is well planned to avoid such incidence [54].

3.2. Experimental measurements of induced electric field

To verify the simulated data, a total of eight coil prototypes were fabricated with two different dimensions, two different winding layers, and different tilting angles. The electric field distributions were measured for each AT coil in air and the commercial 70 mm figure-8 Magstim coil using calibrated high-spatial-resolution vector-field probes. The first coil, named the' Coil-A,' has an inner and outer diameter of 1 cm and 3 cm, respectively, with nine winding layers. The tilting angle ranges from 0° to 60° with a step of 10°. The second coil, named the' Coil-B,' has an inner diameter of 3 cm and an outer diameter of 9 cm with six winding layers with a tilting angle of 40°. Figure S5 in the supplementary data demonstrates the performance of experimental coils and the minimal effect of winding thickness in the depth-spread plot. For comparison, COMSOL simulations and experimental measurements of the electric field decay rate and stimulation hot spot area were conducted in the air. The experimental measurements aim to demonstrate how fast the field diverges generated by each coil. These comparisons need to be done independently of the electric

field strength's absolute values since the absolute values have no effect on the spatial distribution and can be adjusted through the TMS stimulator circuit.

Figure 6 shows FEM simulation and experimental measurement results of electric field distributions at 1.5 cm away from the lowest point of the coils in the air. The results indicate that for all the proposed AT coils, the maximum electric field's location is relatively the same, close to the coil's tilted edge, while for figure-8 coils, it is happening in the center of the coil. This observation further proves the usefulness of the AT coils for multisite stimulation.

Although it is difficult to measure the $S_{1/2}$ directly, one way to properly represent the spread is to check the hot spot's size as defined in the following procedure. First, we scan and obtain the maximum electric field strength at a fixed distance away from the coils. At each distance, hot spot size is defined by measuring the area with the electric field strength above a selected percentage of that measured maximum strength. For example, at the distance of 1.5 cm away from the lowest point of the coils, we define our hot spot size as the areas with an electric field intensity of more than 90% of the measured maximum electric field strength. Although we can choose to set lower percentages, we specified a greater than 90% to avoid scanning a larger area for a smaller percentage without losing fairness and accuracy.

Figure 7(a) shows that tilting the coil's wrapping angle significantly decreases the focal spot size. At a 10° tilted angle, the spot size drops 80% from the flat coil's. The spot size further reduced an additional 70% from around 5.0 cm^2 for the 10° coil to about 1.5 cm^2 for the 60° coil. Thus, the focal spot size of the entire coil-A series is smaller than the figure-8 coil. On the other hand, the 40° tilted coil-B has a slightly bigger focal spot area than the figure-8 coil, which can be overcome if higher tilting angles are used. The argument can be proved by using the coil-A series as an example. The hot spot size reduced 15% from a 40° coil to a 60° coil. If the same effect is applied, the B coil's hot spot size becomes smaller than the figure-8 coil.

The electric field intensity decay rates based on the experimental data and simulations are shown in figures 7(b) and (c), respectively. We first normalized the measured data for an accurate comparison. As shown in these plots, the decay rates gain improvements by increasing the tilting angle. At a depth of 2.5 cm from the coil, the flat coil's decayed remaining value is less than 15.0% for both experimental and simulation data. In contrast, for the 60° tilted coil, the value increases to 25.0%, indicating an improvement of the decay rate. It can also be observed that the 40° tilted coil B has a much slower decay rate than the figure-8 and all other coils. The depth-spread performance of the AT coils is summarized in table 1. The hot spot area of A coils is smaller than the figure-8 coil, while the B coil's hot spot area is comparable to the figure-8 coil. Nevertheless, its decay rate is more than twice slower as the figure-8 coil. More than 40% of field strength remained at a 2.5 cm distance for the B coil than the figure-8 coil with less than 20% left. Additionally, the simulation data in figure 2 shows improved performance for higher tilting angles compared to the 40° tilted coil.

One particularly notable fact is that for the 50° and 60° tilted angles, the small diameter A coils can accomplish better decay rates than the much larger diameter figure-8 coil. This performance shows that the proposed design produces elevated electric field intensity in deeper brain regions due to field redistribution, or more precisely, focusing effect through angle tuning.

3.3. Discussion

The proposed coil design has the main advantage of occupying a much smaller contact surface during the stimulation due to its vertical stacking. For multisite brain stimulation, only one power supply circuit unit is required for the AT coils. Since all the elements are the same with an equal inductance, the combined inductance can easily be adjusted with parallel and serial connections to further improve depth-spread performance and multisite stimulation. The approach of using a uniform building block to construct a composite coil structure provides other benefits. First, mass production of identical small units can help to reduce cost and increase quality. Second, it provides flexibility in designing and implementing a novel generation of TMS tools by merely adjusting the relative geometric locations of these identical building block coils. The single AT coils used in the composite structure can also be adjusted with the tilting angle and the stacking number to match the required stimulation results. Third, the AT coils' simple design allows for easier replacement of possible defective elements in the multi-coil apparatus versus repairing or replacing the whole unit like other reported complicated multisite stimulation structures. Noticeably, compared with the reported or existing complex coil structures designed for deep brain stimulation, our simple four-uniform-AT-coil design has better depth-spread performance, as shown in figure 4. This novel coil design provides a promising new generation of future high depth-spread performance and multisite TMS tools.

With higher inductance (about 65 μH) than figure-8 coils (about 16 μH), the proposed coil design requires the same current to induce equal electric field strength in the brain but requires higher power consumption. Additionally, the proposed coil design wires are flexible, enhancing the sound created by the Lorentz force. One solution is to insulate the flexible wires with epoxy resin. A low value of viscosity for the epoxy resin before solidification is required to fill the space among the wires. Other containment and attenuation methods can further reduce the noise generation of the proposed coils [55]. The experimental noise analysis performed on the proposed coils demonstrated a peak sound pressure level (SPL) of 98 dB(Z) at 100% of the resting motor threshold defined by Koponen *et al* [56]. The analysis showed a 3 dB(Z) increase compared to commercial figure-8 coils [56]. The obtained value is under the safety standard SPL limit of 140 dB(Z) for impulsive sounds [57].

The proposed coils' energy consumption was analyzed based on the neural stimulation threshold of 100 V m^{-1} [58] at 3 cm from the head's surface using the magnetic flux density and magnetic field intensity vectors [59], as demonstrated in table 2. As demonstrated, the AT coils show a significantly smaller half-depth and footprint compared to the commercial figure-8 coils. The analysis indicated that the required energy to reach the threshold increases exponentially by reducing the coil's diameter. The energy consumption of the

16 cm-outer diameter (OD) AT coil is about 40% smaller in comparison to that of the 9 cm-OD AT coil. Compared with the 70 mm figure-8 coil, the 9 cm-OD AT coil requires 3.5 times the energy, and the 16 cm-OD AT requires about 2 times the energy to reach the 100 V m^{-1} thresholds.

In comparison to the 70 mm figure-8 coil, Although the energy requirement of the AT coils is higher, the 9 cm-OD AT coil has a 20% higher penetration depth and 80% smaller footprint, while the four-AT Coils OD-9 (shown in figure 4) has an 88% better penetration depth. This result is expected since the 9 cm-OD AT coil has only a 20% footprint of that of the 70 mm figure-8 coil (coil #31). The 25 mm figure-8 coil has a 30% higher footprint than the 9 cm-OD AT coil and exhibits about 10% higher energy consumption but with much worse depth performance.

It has been shown that increasing the tilting angle has a negative effect on the Energy requirements while causing a significant improvement in the electric field distribution focality and the footprint. In addition, increasing the winding layers has an adverse effect on energy consumption and as demonstrated previously, increasing the winding layers beyond a specific number is ineffective in the performance of the coil. For the complex coil system introduced in our work (figure 4), the depth performance is significantly better than the commercial figure-8 coils, while the required energy is higher.

While many of the proposed coils in this work have shown higher energy requirements in comparison to figure-8 coils, they have a significantly better depth performance to reach deeper regions of the brain. In addition, the energy consumption of all these AT coils are still in the range that can be driven by mainstream commercial TMS power supplies. It should be noted that these coils have not been optimized for energy consumption.

To study the induced maximum electric field intensity (E_{max}), an arbitrary current of 3 kA, an acceptable value for all the commercial TMS stimulators, was applied to the coils demonstrated in table 3. The induced E_{max} at different radial distances from the head surface was analyzed. The data indicate that the proposed coils demonstrate a higher field strength at deeper brain regions. In contrast, conventional 70 mm figure-8 coil shows higher intensities at distances closer to the head surface. This data further verifies the performance of AT coils for stimulation of deeper brain regions.

The supplementary videos demonstrate the capability of the AT coil to induce unilateral movements in anesthetized mice and rats. The voltage of the coil to reach the motor threshold was lower than 1 kV. In the rat stimulation video, the motor response induced by focal stimulation occurs between the 4th and 5th second; in the mice stimulation video, the motor response occurs around the end of the 1st second. In both videos, only the motor cortex region corresponding to the right-side hindlimb is stimulated. The videos demonstrate supra-threshold motor cortex activation of rodents, which not only validates that the probe measurements can be a sufficient method to determine and calibrate coil performance but also shows that the activation spot occupies a very small area in the brain in the millimeter range [60].

The focus of this work is the use of the spherical head model for simulating the electric field distribution. Nevertheless, the spherical model is helpful in benchmarking design metrics such as depth and spread of the electric field, allowing for a standardized comparison between different coil geometries. Future work could use more anatomically accurate head models incorporating realistic cortical folding and white matter anisotropic conductivity. This step would be appropriate when an experimental or clinical application has been identified for the AT coil. The focality and depth performance of the coil is shown to generalize to the realistic head model. The proposed coil design should be optimized for energy consumption and noise generation.

4. Conclusion

In this study, we proposed a novel AT coil structure with a less than 50% smaller footprint and better depth–spread performance than a conventional figure-8 coil. The proposed structure applied to a rodent coil design delivers a significantly small activation spot size and demonstrated single limb motor cortex activation in rodents. This work provides a comprehensive framework to show quantitative depth–spread improvement using different wrapping angles and coil stacking for human brain stimulation. We have shown, theoretically and experimentally, that the AT coils have improved field decay rates to reach deeper regions with a higher field intensity and a reduced field spot size compared with conventional figure-8 coils. The AT coils demonstrated superior performance for multisite stimulation due to their smaller footprint. These coils can also serve as a fundamental building block for more complex coil structures to further improve depth–spread performance.

Acknowledgments

The research was supported by the NSF Grant ECCS-1631820, NIH Grants MH112180, MH108148, MH103222, and a Brain and Behavior Research Foundation grant. It was also partly supported by the Intramural Research Program of the National Institute on Drug Abuse, National Institutes of Health. In addition, Z D is supported by the National Institute of Mental Health Intramural Research Program (ZIAMH002955).

Data availability statement

The data that support the findings of this study are available upon reasonable request from the authors.

References

[1]. Costello A 2011 Repetitive transcranial magnetic stimulation (rTMS) systems—class II special controls guidance for industry and FDA staff

[2]. Caccomo S 2018 FDA permits marketing of transcranial magnetic stimulation for treatment of obsessive compulsive disorder FDA News Release

[3]. Anand S and Hotson J 2002 Transcranial magnetic stimulation: neurophysiological applications and safety Brain Cogn. 50 366–86 [PubMed: 12480484]

[4]. Barker AT and Shields K 2017 Transcranial magnetic stimulation: basic principles and clinical applications in migraine Headache J. Head Face Pain 57 517–24

[5]. Lisanby SH, Luber B, Perera T and Sackeim HA 2000 Transcranial magnetic stimulation: applications in basic neuroscience and neuropsychopharmacology Int. J. Neuropsychopharmacol 3 259–73 [PubMed: 11343603]

[6]. Bullmore E and Sporns O 2009 Complex brain networks: graph theoretical analysis of structural and functional systems Nat. Rev. Neurosci. 10 186–98 [PubMed: 19190637]

[7]. Hutchison RM, Womelsdorf T, Gati JS, Everling S and Menon RS 2013 Resting-state networks show dynamic functional connectivity in awake humans and anesthetized macaques: dynamic functional connectivity Hum. Brain Mapp 34 2154–77 [PubMed: 22438275]

[8]. Koch G and Rothwell JC 2009 TMS investigations into the task-dependent functional interplay between human posterior parietal and motor cortex Behav. Brain Res 202 147–52 [PubMed: 19463695]

[9]. Rothwell JC 2011 Using transcranial magnetic stimulation methods to probe connectivity between motor areas of the brain Hum. Mov. Sci 30 906–15 [PubMed: 21056490]

[10]. Koganemaru S, Mima T, Nakatsuka M, Ueki Y, Fukuyama H and Domen K 2009 Human motor associative plasticity induced by paired bihemispheric stimulation: paired bihemispheric stimulation induces motor plasticity J. Physiol. 587 4629–44 [PubMed: 19687124]

[11]. Buch ER, Johnen VM, Nelissen N, O'Shea J and Rushworth MFS 2011 Noninvasive associative plasticity induction in a corticocortical pathway of the human brain J. Neurosci. 31 17669–79 [PubMed: 22131427]

[12]. Lu M-K, Tsai CH and Ziemann U 2012 Cerebellum to motor cortex paired associative stimulation induces bidirectional STDP-like plasticity in human motor cortex Front. Hum. Neurosci 6 260 [PubMed: 23049508]

[13]. Takeuchi N, Tada T, Toshima M and Ikoma K 2010 Correlation of motor function with transcallosal and intracortical inhibition after stroke J. Rehabil. Med 42 962–6 [PubMed: 21031294]

[14]. Schmitt A, Hasan A, Gruber O and Falkai P 2011 Schizophrenia as a disorder of disconnectivity Eur. Arch. Psychiatry Clin. Neurosci 261 150–4

[15]. Farzan F, Vernet M, Shafi MMD, Rotenberg A, Daskalakis ZJ and Pascual-Leone A 2016 Characterizing and modulating brain circuitry through transcranial magnetic stimulation combined with electroencephalography Front. Neural Circuits 10 73 [PubMed: 27713691]

[16]. Cash RFH, Cocchi L, Anderson R, Rogachov A, Kucyi A, Barnett AJ, Zalesky A and Fitzgerald PB 2019 A multivariate neuroimaging biomarker of individual outcome to transcranial magnetic stimulation in depression Hum. Brain Mapp 40 4618–29 [PubMed: 31332903]

[17]. Groppa S, Werner-Petroll N, Münchau A, Deuschl G, Ruschworth MF and Siebner HR 2012 A novel dual-site transcranial magnetic stimulation paradigm to probe fast facilitatory inputs from ipsilateral dorsal premotor cortex to primary motor cortex Neuroimage 62 500–9 [PubMed: 22626848]

[18]. Parmigiani S, Barchiesi G and Cattaneo L 2015 The dorsal premotor cortex exerts a powerful and specific inhibitory effect on the ipsilateral corticofacial system: a dual-coil transcranial magnetic stimulation study Exp. Brain Res 233 3253–60 [PubMed: 26233241]

[19]. Barker AT, Jalinous R and Freeston IL 1985 Non-invasive magnetic stimulation of human motor cortex Lancet 325 1106–7

[20]. Ueno S, Tashiro T and Harada K 1988 Localized stimulation of neural tissues in the brain by means of a paired configuration of time-varying magnetic fields J. Appl. Phys 64 5862–4

[21]. Roth Y, Zangen A and Hallett M 2002 A coil design for transcranial magnetic stimulation of deep brain regions J. Clin. Neurophysiol 19 361–70 [PubMed: 12436090]

[22]. Gomez LJ, Goetz SM and Peterchev AV 2018 Design of transcranial magnetic stimulation coils with optimal trade-off between depth, focality, and energy J. Neural Eng. 15 046033 [PubMed: 29855433]

[23]. Meng Y, Hadimani RL, Crowther LJ, Xu Z, Qu J and Jiles DC 2015 Deep brain transcranial magnetic stimulation using variable "Halo coil" system J. Appl. Phys. 117 17B305

[24]. Rastogi P, Tang Y, Zhang B, Lee EG, Hadimani RL and Jiles DC 2017 Quadruple butterfly coil with passive magnetic shielding for focused transcranial magnetic stimulation IEEE Trans. Magn 53 5400305

[25]. Deng Z-D, Lisanby SH and Peterchev AV 2013 Electric field depth–focality tradeoff in transcranial magnetic stimulation: simulation comparison of 50 coil designs Brain Stimul. 6 1–13 [PubMed: 22483681]

[26]. Basser PJ, Wijesinghe RS and Roth BJ 1992 The activating function for magnetic stimulation derived from a three-dimensional volume conductor model IEEE Trans. Biomed. Eng 39 1207–10 [PubMed: 1487283]

[27]. Jalinous R 1991 Technical and practical aspects of magnetic nerve stimulation J. Clin. Neurophysiol 8 10–25 [PubMed: 2019644]

[28]. Roth BJ, Cohen LG and Hallett M 1994 The electric field induced during magnetic stimulation Electroencephalogr. Clin. Neurophysiol 43 268–78

[29]. Heller L and van Hulsteyn D B 1992 Brain stimulation using electromagnetic sources: theoretical aspects Biophys. J. 63 129–38 [PubMed: 1420862]

[30]. Deng Z-D, Lisanby SH and Peterchev AV 2014 Coil design considerations for deep transcranial magnetic stimulation Clin. Neurophysiol 125 1202–12 [PubMed: 24411523]

[31]. Salinas FS, Lancaster JL and Fox PT 2009 3D modeling of the total electric field induced by transcranial magnetic stimulation using the boundary element method Phys. Med. Biol. 54 3631 [PubMed: 19458407]

[32]. Wagner TA, Zahn M, Grodzinsky AJ and Pascual-Leone A 2004 Three-dimensional head model simulation of transcranial magnetic stimulation IEEE Trans. Biomed. Eng 51 1586–98 [PubMed: 15376507]

[33]. Bagherzadeh H and Choa F 2019 Effect of coil size on transcranial magnetic stimulation (TMS) focality Smart Biomed. Physiol. Sens. Technol. XVI vol 11020 (International Society for Optics and Photonics) p 110200Z

[34]. Al-Mutawaly N, de Bruin H and Findlay D 2001 Magnetic nerve stimulation: field focality and depth of penetration 2001 Conf. Proc. 23rd Annu. Int. Conf. IEEE Eng. Med. Biol. Soc. vol 1 (IEEE) pp 877–80

[35]. Wei X, Li Y, Yi G, Lu M, Wang J and Zhang Z 2017 The comparison of electric fields distribution applying various coil configurations in deep transcranial magnetic stimulation 2017 10th Int. Congr. Image Signal Process. Biomed. Eng. Inform. CISP-BMEI (IEEE) pp 1–5

[36]. Bagherzadeh H and Choa F-S 2021 Implementation of novel TMS coils for multisite brain stimulations Smart Biomed. Physiol. Sens. Technol XVIII ed Cullum BM, McLamore ES and Kiehl D (United States: SPIE) p 25

[37]. Meng Q, Hong E and Choa F-S 2017 Transcranial magnetic stimulation (TMS) coil designing for high electromagnetic field gradient generation Brain Stimul. Basic Transl. Clin. Res. Neuromodulation 10 499

[38]. Lisanby SH, Gutman D, Luber B, Schroeder C, Sackeim HA and Sham TMS 2001 intracerebral measurement of the induced electrical field and the induction of motor-evoked potentials Biol. Psychiatry 49 460–3 [PubMed: 11274658]

[39]. Wagner T, Gangitano M, Romero R, Théoret H, Kobayashi M, Anschel D, Ives J, Cuffin N, Schomer D and Pascual-Leone A 2004 Intracranial measurement of current densities induced by transcranial magnetic stimulation in the human brain Neurosci. Lett. 354 91–94 [PubMed: 14698446]

[40]. Maccabee PJ, Amassian VE, Eberle LP and Cracco RQ 1993 Magnetic coil stimulation of straight and bent amphibian and mammalian peripheral nerve *in vitro*: locus of excitation J. Physiol. 460 201–19 [PubMed: 8487192]

[41]. Meng Q et al. 2018 A novel transcranial magnetic stimulator for focal stimulation of rodent brain Brain Stimul. Basic Transl. Clin. Res. Neuromodulation 11 663–5

[42]. Lu H, Meng Q, Peng K, Cermak S, Stein E, Yang Y and Choa F 2019 Focal transcranial magnetic stimulation (TMS) of the rat brain: coil design, c-fos mapping and electrophysiology Brain Stimul. 12 555–6

[43]. Cermak S, Meng Q, Peng K, Baldwin S, Mejías-Aponte CA, Yang Y and Lu H 2020 Focal transcranial magnetic stimulation in awake rats: enhanced glucose uptake in deep cortical layers J. Neurosci. Methods 339 108709 [PubMed: 32259609]

[44]. Hong LE and Choa F-S 2019 Methods and systems for controlling magnetic fields and magnetic field induced current US Patent 10518098

[45]. Meng Q et al. 2018 Development of focused transcranial magnetic stimulation for rodents by copper-array shields IEEE Trans. Magn 54 1–4

[46]. de Lara LIN, Daneshzand M, Mascarenas A, Paulson D, Pratt K, Okada Y, Raij T, Makarov SN and Nummenmaa A 2021 A 3-axis coil design for multichannel TMS arrays NeuroImage 224 117355 [PubMed: 32916290]

[47]. Koponen LM, Nieminen JO and Ilmoniemi RJ 2018 Multi-locus transcranial magnetic stimulation—theory and implementation Brain Stimul. 11 849–55 [PubMed: 29627272]

[48]. Nummenmaa A, Stenroos M, Ilmoniemi RJ, Okada YC, Hämäläinen MS and Raij T 2013 Comparison of spherical and realistically shaped boundary element head models for transcranial magnetic stimulation navigation Clin. Neurophysiol 124 1995–2007 [PubMed: 23890512]

[49]. Eaton H 1992 Electric field induced in a spherical volume conductor from arbitrary coils: application to magnetic stimulation and MEG Med. Biol. Eng. Comput. 30 433–40 [PubMed: 1487945]

[50]. Meng Q, Daugherty M, Patel P, Trivedi S, Du X, Hong E and Choa F-S 2018 High-sensitivity and spatial resolution transient magnetic and electric field probes for transcranial magnetic stimulator characterizations Instrum. Sci. Technol. 46 502–18

[51]. Lee EG, Rastogi P, Hadimani RL, Jiles DC and Camprodon JA 2018 Impact of non-brain anatomy and coil orientation on inter- and intra-subject variability in TMS at midline Clin. Neurophysiol 129 1873–83 [PubMed: 30005214]

[52]. Lee EG et al. 2016 Investigational effect of brain-scalp distance on the efficacy of transcranial magnetic stimulation treatment in depression IEEE Trans. Magn 52 5000804

[53]. Hasgall PA, Di Gennaro F, Baumgartner C, Neufeld E, Lloyd B, Gosselin MC, Payne D, Klingenböck A and Kuster N 2018 It'is database for thermal and electromagnetic parameters of biological tissues (10.13099/VIP21000-04-0)

[54]. Ni Z, Charab S, Gunraj C, Nelson AJ, Udupa K, Yeh I-J and Chen R 2011 Transcranial magnetic stimulation in different current directions activates separate cortical circuits J. Neurophysiol. 105 749–56 [PubMed: 21148098]

[55]. Koponen LM, Goetz S and Peterchev AV 2021 Double-containment coil with enhanced winding mounting for transcranial magnetic stimulation with reduced acoustic noise *IEEE Trans*. Biomed. Eng. 68 1

[56]. Koponen LM, Goetz SM, Tucci DL and Peterchev AV 2020 Sound comparison of seven TMS coils at matched stimulation strength Brain Stimul. 13 873–80 [PubMed: 32289720]

[57]. Embleton TFW 1997 Technical assessment of upper limits on noise in the workplace Noise News Int. 5 203–16

[58]. Epstein CM, Schwartzberg DG, Davey KR and Sudderth DB 1990 Localizing the site of magnetic brain stimulation in humans Neurology 40 666 [PubMed: 2320243]

[59]. Haus HA and Melcher JR 1989 Electromagnetic Fields and Energy (Englewood Cliffs, NJ: Prentice Hall)

[60]. Catania KC and Remple MS 2002 Somatosensory cortex dominated by the representation of teeth in the naked mole-rat brain Proc. Natl Acad. Sci 99 5692–7 [PubMed: 11943853]

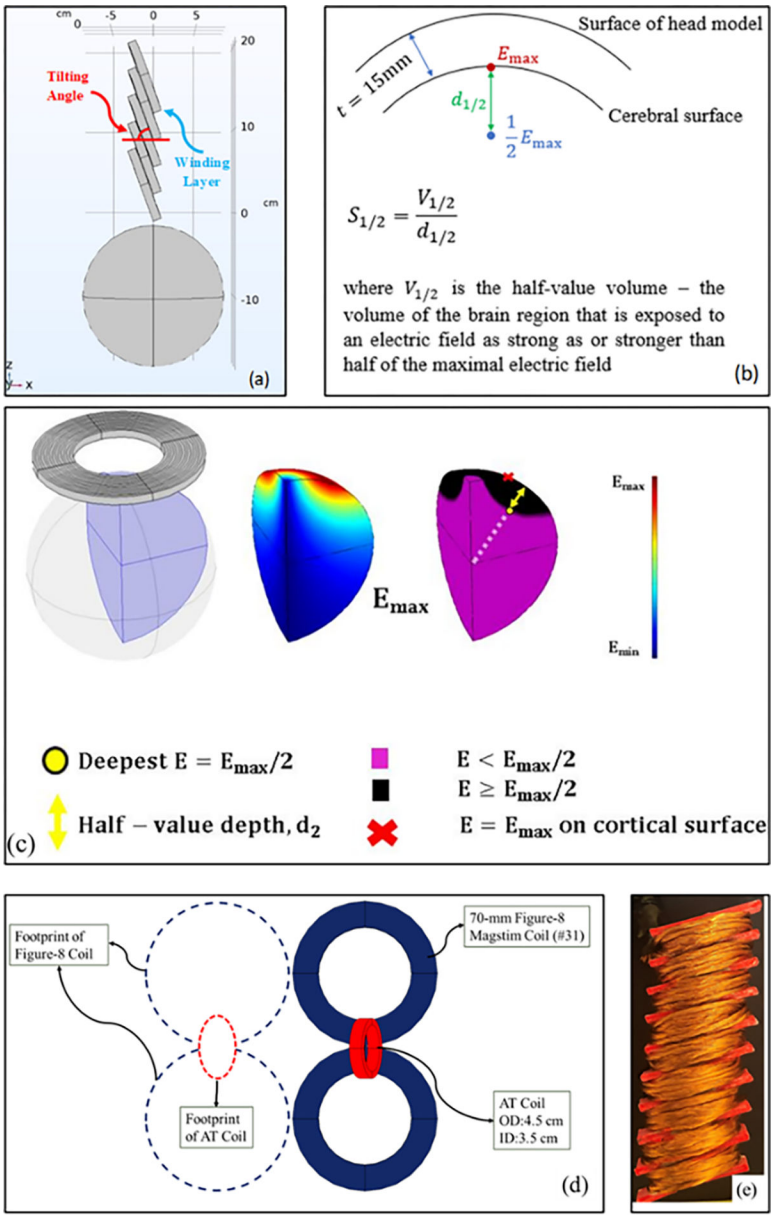

Figure 1.

(a) Illustration of side-view for the proposed angle-tuned TMS coil with five winding layers located above a homogenous and spherical head model, (b) The definitions of the half-value depth ($d_{1/2}$), half-value volume ($V_{1/2}$), and half-value spread ($S_{1/2}$) used for the estimation of the depth-spread characteristics for the proposed coils; The cerebral cortex is defined 1.5 cm below the surface of the head model. The half-value depth is defined as the radial distance from the cortical surface to the deepest point where the electric field strength is half of the maximum field strength on the cortical surface, (c) Induced electric field in the head model. The volume and depth of the electric field define half-value depth, half-value volume, and half-value spread, (d) A plan view of the definition of the footprint. For the figure-8 coil (shown in blue), the footprint involves two circular coils with an outer diameter of 8.7 cm for each and is around 120 cm^2 (dotted blue lines). In contrast, for the AT coil (shown in

red), this value is calculated by multiplying the coil's surface area by the cosine of the tilting angle. The footprint for a single 4.5 cm outer diameter is around 5.5 cm^2 (dotted red lines), (e) Fabricated angle-tuned coil for experimental measurements with nine winding layers wrapped over a 3D printed coil holder. The fabricated coil has an inner and outer diameter of 1 cm and 3 cm, respectively, with a tilting angle of 20°.

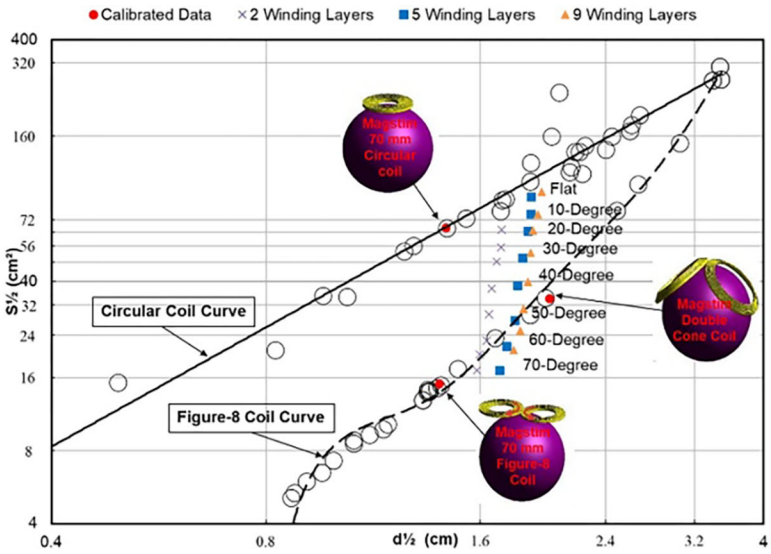

Figure 2.

Depth-spread performance of the proposed coils; Effect of tilting angle and accumulation of wire wrapped coils on $S_{1/2}$ and $d_{1/2}$. The circles represent the locations of the previously studied coils by Deng *et al* [25]. The solid and dashed lines show the best-fit curves for the circular and figure-8 types of coils, respectively. The red dots are the calibrations performed in this study in COMSOL to validate the simulation technique. The AT coils have an inner and outer diameter of 8 cm and 9 cm, respectively, with tilting angles ranging from 0° to 70° with 10° steps and winding layers of 2, 5, and 9.

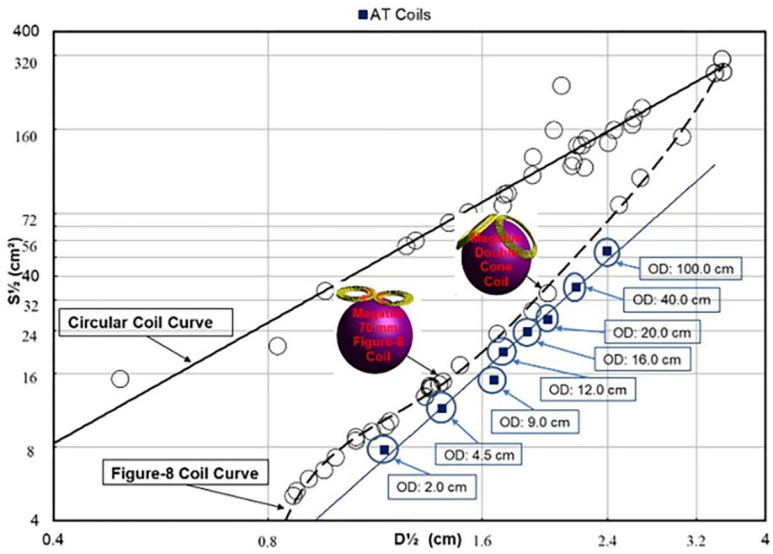

Figure 3.

Effect of the coil's outer diameter on the depth-spread performance of the proposed coils. In the plot, the 'O.D.' represents the outer diameter of the studied coil. The outer diameter of the single AT coils varies from 2 cm to 100 cm, with the winding width kept constant at 1 cm, meaning that the inner diameter is 1 cm smaller than the outer diameter.

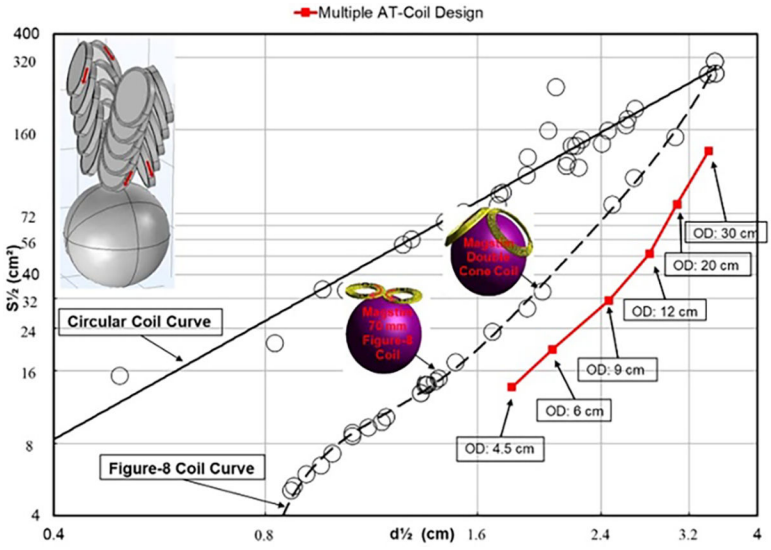

Figure 4.

Effectiveness of using multiple AT coils as pairs for improving the depth–spread. The composite coil structure is shown in the top left corner, with the red arrows showing each coil's current direction. In this design, two 80° tilted coils with an internal angle of 20° form a pair; the proposed coil design is comprised of two of these pairs with opposite polarities and an internal angle of 60°, and the coil O.D. changes from 4.5 to 30 cm with 1 cm winding width.

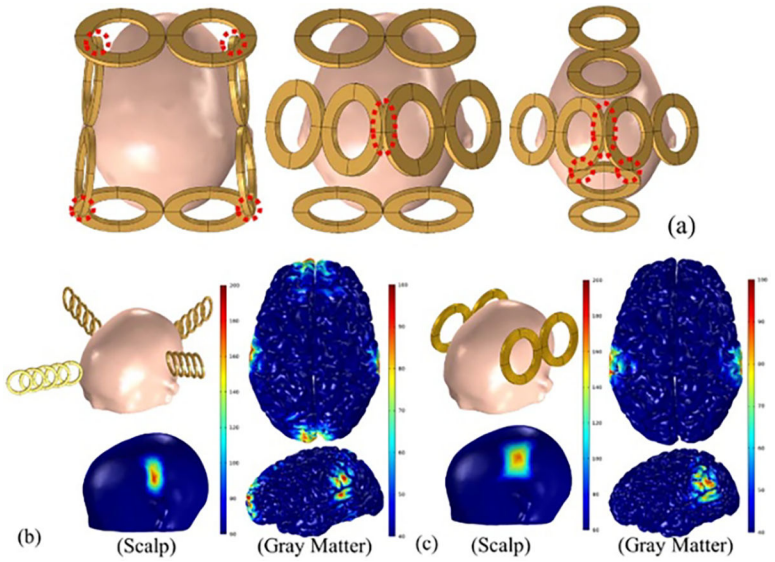

Figure 5.

Multisite stimulation using AT coils in comparison to figure-8 coils in a realistic head model. The AT coils used in this analysis had an O.D. of 4.5 cm and an I.D. of 3.5 cm and were compared to the Magstim 70 mm figure-8 coil. Different views of the gray matter are shown to better understand the coils' performance. All the units are V m^{-1}. (a) Different examples of four figure-8 coils placed on the scalp to stimulate four brain regions. The inflexibility of the coils to stimulate the desired brain regions is clearly illustrated. The overlapping conflicts between coils are marked with red circles. (b) Stimulation locations of four AT coils relative to the head model and the induced electric field distributions with color-coded intensities on the scalp and the gray matter, (c) Stimulation locations and results of dual figure-8 coils.

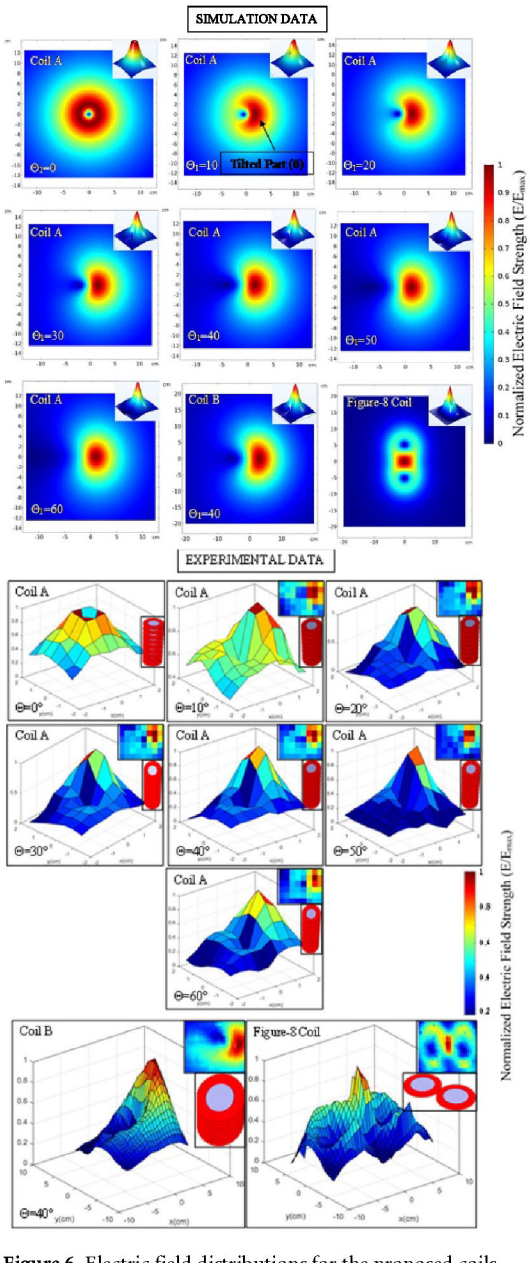

Figure 6.

Electric field distributions for the proposed coils with different tilting angles based on the simulations and experimental measurements; Both the 2D and 3D distributions of the electric field were simulated. All the experimental measurements were performed at a 1.5 cm distance from the coil's lowest point with 5 mm lateral steps using calibrated vector-field probes. All the data is normalized to the highest electric field intensity. In the experimental data, the scanned area for the coil-B and the figure-8 coil is larger than the coil-A series due to their larger size, which resulted in more pixels for the two coils.

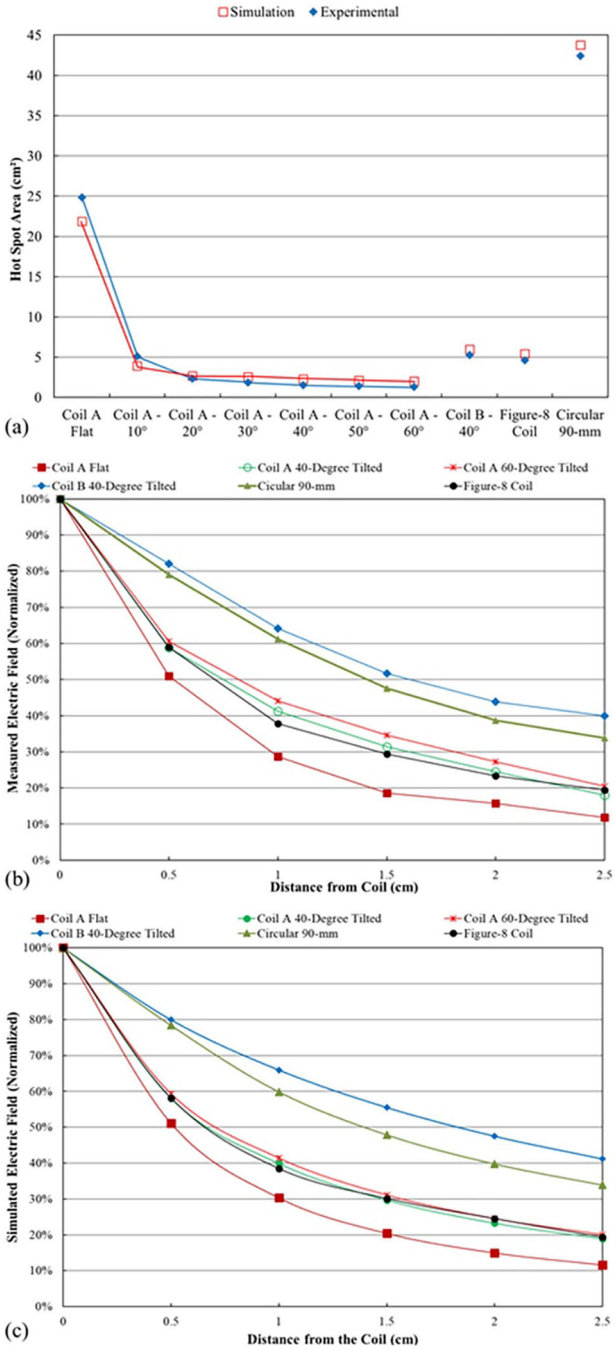

Figure 7.

(a) Hot spot size for experimental data and simulations. The hot spot size is measured and simulated at 1.5 cm away from the lowest point of the coil, (b) electric field intensity decay rate (in percentage) as a function of depth for the experimental measurements, (c) electric field intensity decay rate (in percentage) as a function of depth for FEM simulations. The presented distance in this figure is from the surface of the coil in the air. In contrast, in Deng *et al* [25], the distance is considered from the cortex, which is 2 cm away from the coil's surface. Considering the same concept for this figure (from 2 cm to 2.5 cm) indicates about

10% improvement from the figure-8 coil to Coil B, which matches the data obtained in the first part of this study in figure 2 through 4.

Table 1.

AT coil's performance in detail; the hot spot area and the induced electric field intensity decay rates from experimental measurements and FEM simulations. The data indicated here is obtained through experimental and FEM simulations in air, as explained in section 3.2.

		Hot Spot Area (cm^2)		Remaining % @ 2.5 cm	
Coil Type	**Tilting Angle (°)**	**Measured Value**	**Simulated Value**	**Measured Value**	**Simulated Value**
Coil A	Flat	24.88	21.89	11.80	11.60
	10	5.13	3.90	13.60	14.10
	20	2.34	2.70	15.60	16.10
	30	1.85	2.57	16.70	17.90
	40	1.52	2.58	17.90	18.90
	50	1.41	2.13	19.00	19.60
	60	1.30	2.01	20.50	20.10
Coil B	40	5.28	5.98	40.00	41.10
Figure-8 coil		4.61	5.44	19.40	19.30

J Neural Eng. Author manuscript; available in PMC 2023 November 14.

Table 2.

Energy consumption of the proposed coil designs in comparison with that of commercial coils. The energy required for a neural stimulation threshold of 100 V m^{-1} at 3 cm from the head's surface, along with the footprint and the half penetration depth of each coil. Different AT coil parameters have been studied to demonstrate the performance trend of these coils.

Coil Type	$d_{1/2}$ (cm)	Footprint (cm^2)	Energy (J)
Commercial Coils			
25 mm Figure-8 (#25)	0.96	27.71	670
70 mm Figure-8 (#31)	1.41	118.9	170
Effect of Tilting Angle (OD-9, 5 Windings)			
AT Single 10°	1.78	62.65	160
AT Single 40°	1.7	59.78	320
AT Single 70°	1.61	21.76	610
Effect of Winding Layers (OD-9, 70° Tilted)			
AT Single—2 Windings	1.55	21.76	390
AT Single—5 Windings	1.61	21.76	610
AT Single—9 Windings	1.69	21.76	960
Effect of Outer Diameter (5 Windings, 70° Tilted)			
AT Single—OD-4.5	1.4	5.44	1090
AT Single—OD-9	1.61	21.76	610
AT Single—OD-16	1.85	68.77	360
Effect of Outer Diameter (4-Coil System)			
4-AT Coils OD-6	2.05	38.68	1730
4-AT Coils OD-9	2.46	87.04	1470

Table 3.

Maximum electric field intensity (E_{max}) of the proposed coil designs. Three coils' maximum electric field intensity was analyzed using an arbitrary current of 3 kA applied to each coil. The small figure-8 coil has an outer diameter of 1.86 cm for each ring, making the footprint equivalent to the AT OD-9 cm 70°.

Radial Distance from Head Surface (cm)	Maximum Electric Field Intensity (E_{max})		
	70 mm Figure-8 (#31)	AT OD-9 cm 70°	Small Figure-8
2	111.54	105.96	24.99
2.5	87.60	84.18	17.43
3	68.52	69.27	11.94
3.5	53.19	58.11	8.25
4	41.19	47.82	5.76
4.5	31.83	39.36	4.11
5	24.27	32.72	2.88